

# AEDR: Training-Free AI-Generated Image Attribution via Autoencoder Double-Reconstruction

Chao Wang<sup>1</sup>, Kejiang Chen<sup>1\*</sup>, Zijin Yang<sup>1</sup>, Yaofei Wang<sup>2</sup>, Weiming Zhang<sup>1</sup>

<sup>1</sup>University of Science and Technology of China

<sup>2</sup>Hefei University of Technology

{chaowang0708@mail., chenkj@, bsmhmmlf@mail., zhangwm@}ustc.edu.cn  
wyf@hfut.edu.cn

## Abstract

The rapid advancement of image-generation technologies has made it possible for anyone to create photorealistic images using generative models, raising significant security concerns. To mitigate malicious use, tracing the origin of such images is essential. Reconstruction-based attribution methods offer a promising solution, but they often suffer from reduced accuracy and high computational costs when applied to state-of-the-art (SOTA) models. To address these challenges, we propose AEDR (AutoEncoder Double-Reconstruction), a novel training-free attribution method designed for generative models with continuous autoencoders. Unlike existing reconstruction-based approaches that rely on the value of a single reconstruction loss, AEDR performs two consecutive reconstructions using the model’s autoencoder, and adopts the ratio of these two reconstruction losses as the attribution signal. This signal is further calibrated using the image homogeneity metric to improve accuracy, which inherently cancels out absolute biases caused by image complexity, with autoencoder-based reconstruction ensuring superior computational efficiency. Experiments on eight top latent diffusion models show that AEDR achieves 25.5% higher attribution accuracy than existing reconstruction-based methods, with requiring only 1% of the computational time.

## 1 Introduction

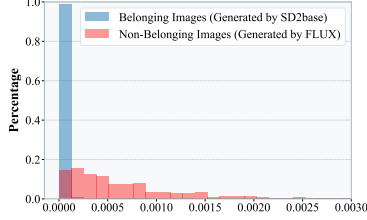
Latent diffusion models [22, 32, 39] have emerged as the dominant paradigm in image generation due to their exceptional capabilities in producing high-resolution and photorealistic content. Their effectiveness in modeling complex data distributions has facilitated numerous applications across diverse fields, such as digital art, advertising, and virtual reality [8]. Recent models such as Stable Diffusion 3.5 [13] enable rapid and controllable image synthesis, supporting a wide range of real-world applications.

While the powerful capabilities of AI-generated images are widely embraced, concerns about potential misuse are growing [2, 4, 27, 51]. For instance, unscrupulous vendors may repurpose outputs from third-party models as their own, falsely promoting model performance and thereby misleading consumers while undermining fair market competition. Furthermore, malicious actors can present outputs from commercial models [1] as original creations to gain reputational and financial advantages, flagrantly violating the intellectual property rights of model developers [23]. Reliable image origin attribution, therefore, has become indispensable for accurately identifying the responsible entities behind such generated content.

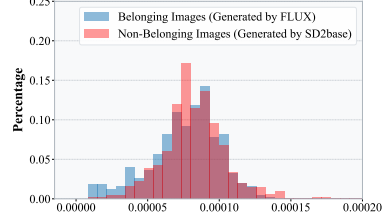
Existing image attribution methods generally fall into three primary categories. Watermark-based methods [25, 28, 38, 44–46] embed invisible or semi-visible marks during image generation, enabling

---

\*Corresponding author.

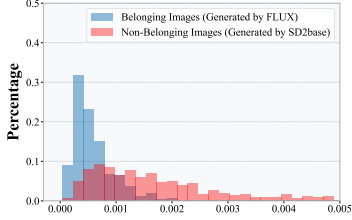


(a) Gradient-based reconstruction using SD2base.

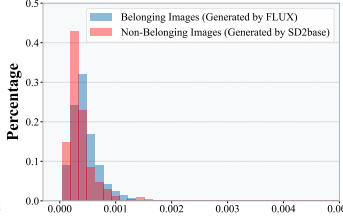


(b) Gradient-based reconstruction using FLUX.

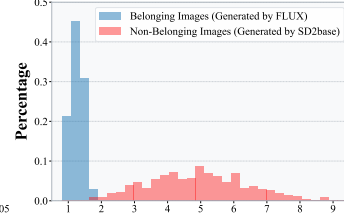
Figure 1: Gradient-based reconstruction methods exhibit different loss distributions.



(a) Distribution of the first loss.



(b) Distribution of the second loss.



(c) Distribution of the loss ratio.

Figure 2: Double-Reconstruction loss variation and loss ratio.

attribution through watermark detection. Fingerprint-based methods [9, 48–50] introduce model-specific signatures during training or by modifying the architecture, and rely on supervised classifiers to detect these fingerprints in generated images. However, both methods require additional operations during training or inference, which may degrade the visual quality of the generated images. In contrast, passive detection approaches, which do not require modifications to the training process of target models, are more practical and acceptable in real-world applications. Among these, reconstruction-based methods [42, 43] have achieved excellent performance. They use gradient information from the generative model to reconstruct the input image, using the reconstruction loss between the original and reconstructed images serving as the attribution signal. These methods do not modify model parameters or the generation pipeline, and thus preserve generative performance, making them one of the most promising approaches for image attribution.

Existing gradient-based reconstruction methods typically follow this observation: images that belong to the target model generally exhibit lower reconstruction losses than non-belonging images (see Figure 1a). Thus, the two types of images can be distinguished based on a single reconstruction loss value. However, with increasingly powerful generative models such as FLUX [22], these methods [42, 43] tend to produce extremely low reconstruction losses for both belonging and non-belonging images, causing significant overlap in the loss distributions and thereby reducing attribution accuracy (see Figure 1b). Moreover, the gradient-guided process is computationally expensive and complex, making these methods impractical for real-world applications.

To address these limitations, we prefer to adopt autoencoder-based reconstruction as the foundation for an efficient attribution. However, using reconstruction loss directly is susceptible to the inherent complexity of the input image [6, 34]: Images with simple textures naturally have lower reconstruction loss, while those with complex textures correspondingly have higher reconstruction loss. To mitigate this bias introduced by image complexity, we propose an attribution method based on the loss ratio across double-reconstructions by the autoencoder. The key insight is that the autoencoder has learned to capture representative features of samples from the training distribution. As illustrated in Figure 2a and Figure 2b, we observe that when the autoencoder reconstructs a belonging image twice, the resulting reconstruction losses are nearly identical, since the image lies within the model’s distribution. In contrast, for the non-belonging image, which initially lies outside the model distribution, the first reconstruction effectively projects it into the distribution, leading to a noticeably lower loss in the second reconstruction. Consequently, if we compute the ratio of the first to the second reconstruction loss, the value tends to be close to 1 for belonging images, but significantly greater than 1 for non-belonging ones (see Figure 2c).

Motivated by this insight, we propose an image attribution method based on **AutoEncoder Double-Reconstruction**, namely **AEDR**. Unlike existing gradient-guided approaches that utilize single reconstruction loss, AEDR employs the loss ratio from double reconstructions, calibrated by an image homogeneity metric. This approach mitigates discrepancies arising from image texture complexity. Additionally, we implement a Kernel Density Estimation (KDE) method [19] for adaptive threshold selection, which assumes no prior knowledge of underlying data distributions, thereby enhancing the adaptability across diverse generative models. Our contributions are summarized as follows:

- We reveal that existing reconstruction-based generated image attribution methods, which rely on the single reconstruction loss, face significant challenges when applied to SOTA generative models. We identify a key discrepancy: under autoencoder-based double-reconstruction, belonging images show significantly higher latent feature consistency across their reconstructions than non-belonging ones.
- We propose AEDR, an attribution method that leverages the ratio of losses from two successive reconstructions and calibrates it based on image homogeneity. AEDR performs direct reconstruction using the model’s autoencoder, eliminating the need for gradient-based optimization or additional training.
- Extensive experiments on eight state-of-the-art or widely used generative models demonstrate that AEDR improves the attribution accuracy by an average of 25.5% and reduces the attribution time to just 1% of the best-performing baseline.

## 2 Related Work

**Image Generative Models.** Early frameworks like Generative Adversarial Networks (GANs) [15], Variational Autoencoders (VAEs) [20], and autoregressive methods such as PixelCNN [40] laid the groundwork for realistic image synthesis. However, diffusion models have recently become the leading approach. Denoising Diffusion Probabilistic Models (DDPMs) [17] achieve remarkable image fidelity by iteratively adding and reversing Gaussian noise, using simplified objectives and U-Net architectures. Building on this, Latent Diffusion Models (LDMs) [35] improved efficiency by processing diffusion within a compact latent space, enabling rapid, high-resolution image generation with significantly lower computational requirements. Many SOTA image generative models, such as Stable Diffusion [13, 30] and FLUX [22], also follow this paradigm.

**Detection of AI-Generated Images.** As generative images grow increasingly photorealistic, the need for reliable detection is increasing [3]. Early work by Marra combined CycleGAN with steganalysis to identify GAN-generated images, laying a foundation for this field. Most existing methods frame the task as a binary classification problem, distinguishing between real and generated images. These approaches often rely on discriminative texture features [5, 16, 21, 24, 31] or frequency domain signals [7, 11, 12, 14, 18] as core detection cues. Recent approaches such as AEROBLADE [34] and HFI [6] adopt reconstruction losses via autoencoders and use LPIPS as a detection metric. Although these methods demonstrate promising performance in generative image detection, they do not address the more challenging task of origin attribution, which is the focus of this paper.

**Origin Attribution of Generated Images.** Current methods for attributing the source of the generated images can be broadly classified into three types: watermark-based methods [25, 28, 38, 44–46], fingerprint-based methods [9, 48–50], and reconstruction-based methods [42, 43]. Watermark-based methods embed model-specific information into the generated image and retrieve this information during detection to identify the source. Fingerprint-based methods inject unique patterns into the model during training and rely on dedicated classifiers for attribution. However, both approaches require additional intervention during image generation or model training and may compromise the quality of the generated images. In contrast, reconstruction-based methods enable origin attribution without the need for any extra operations. For example, both RONAN [42] and LatentTracer [43] adopt gradient-based reconstruction approaches, using the reconstruction loss between the reconstructed and original images as the attribution signal. These methods have been shown to be effective for certain generative models; however, their attribution accuracy degrades significantly as model performance increases.

### 3 Problem Formulation

In this section, we formally define the key problems related in this work as follows:

**Definition 1 (Images Attributed to the Target Model).** Given an image generative model  $\mathcal{M} : \mathcal{I} \rightarrow \mathcal{X}_{\mathcal{M}}$ , where  $\mathcal{I}$  is the input space and  $\mathcal{X}_{\mathcal{M}} \subset \mathcal{X}$  denotes the subset of images produced by  $\mathcal{M}$ , with  $\mathcal{X}$  representing the full image space. A test image  $x$  is classified as a belonging image if and only if  $x \in \mathcal{X}_{\mathcal{M}}$ ; if  $x \notin \mathcal{X}_{\mathcal{M}}$ , it is classified as a non-belonging image.

**Definition 2 (Autoencoder-Based Reconstruction).** The autoencoder  $\mathcal{R}$  of the target model  $\mathcal{M}$  comprises an encoder  $\mathcal{E} : \mathcal{X} \rightarrow \mathcal{Z}$  and a decoder  $\mathcal{D} : \mathcal{Z} \rightarrow \mathcal{X}$ , where  $\mathcal{X}$  denotes the pixel space and  $\mathcal{Z}$  denotes the latent space. The autoencoder-based reconstruction process is defined as  $x^* = \mathcal{R}(x) = \mathcal{D}(z) = \mathcal{D}(\mathcal{E}(x))$ , where  $x \in \mathcal{X}$  is the input image,  $z = \mathcal{E}(x)$  is its latent representation, and  $x^* = \mathcal{D}(z)$  is the reconstructed image.

**Definition 3 (Double-Reconstruction Based Origin Attribution).** Given a test image  $x$  and a generative model  $\mathcal{M}$  with autoencoder  $\mathcal{R}$ , two rounds of encoding-decoding yield reconstructions  $x^* = \mathcal{D}(\mathcal{E}(x))$  and  $x^{**} = \mathcal{D}(\mathcal{E}(x^*))$ . The attribution signal  $t'$  is defined as the ratio of the reconstruction losses  $\mathcal{L}(x^*, x)$  and  $\mathcal{L}(x^{**}, x^*)$ , further calibrated by an image homogeneity metric. If and only if  $t' < \tau$ , where  $\tau$  is a predefined threshold,  $x$  is classified as a belonging image; otherwise, it is considered a non-belonging image.

### 4 Method

This section presents a detailed overview of the proposed method, AEDR. The process begins by reconstructing the input image twice using an autoencoder, from which the reconstruction loss ratio is computed. To enhance robustness, this ratio is calibrated with an image homogeneity metric, resulting in the generation of the attribution signal. Finally, the attribution signal is compared against a precomputed threshold to determine the final attribution outcome. The overall AEDR framework is illustrated in Figure 3.

#### 4.1 Goal and Capability of the Detector

**Goal.** The detector aims to enable fast and accurate origin attribution for AI-generated images without modifying the training or inference of the target model  $\mathcal{M}$ , and without applying any post-processing to its outputs. Formally, the attribution is defined as a binary function  $F : \{\mathcal{M}, x\} \rightarrow \{0, 1\}$ , where  $F(\mathcal{M}, x) = 0$  denotes that image  $x$  is attributed to model  $\mathcal{M}$  (belonging image), and  $F(\mathcal{M}, x) = 1$  indicates that it is not (non-belonging image).

**Capability.** The detector has access only to the autoencoder  $\mathcal{R}$  of the target model  $\mathcal{M}$ , enabling reconstruction via encoder and decoder queries. In contrast to methods like RONAN [42] and LatentTracer [43], which require full white-box access and gradient information, AEDR operates exclusively through autoencoder interaction, making it more suitable for scenarios with strict security constraints or limited computational resources.

#### 4.2 Double-Reconstruction Based on Autoencoder

The specific workflow is as follows: Given the autoencoder  $\mathcal{R}$  of the target model  $\mathcal{M}$  and a test image  $x$ , we perform the following two reconstruction steps.

First Reconstruction:

$$x^* = \mathcal{R}(x) = \mathcal{D}(\mathcal{E}(x)), \quad \mathcal{L}_1 = \mathcal{L}(x^*, x). \quad (1)$$

Second Reconstruction:

$$x^{**} = \mathcal{R}(x^*) = \mathcal{D}(\mathcal{E}(x^*)), \quad \mathcal{L}_2 = \mathcal{L}(x^{**}, x^*). \quad (2)$$

Here,  $x^*$  and  $x^{**}$  denote the reconstructed images obtained from the first and second passes through the autoencoder  $\mathcal{R}$ . The corresponding reconstruction losses are denoted by  $\mathcal{L}_1$  and  $\mathcal{L}_2$ , both computed using mean squared error (MSE). The advantage of using MSE is demonstrated in Experiment 5.5. AEDR focuses on analyzing the trend of variation in reconstruction losses for the test

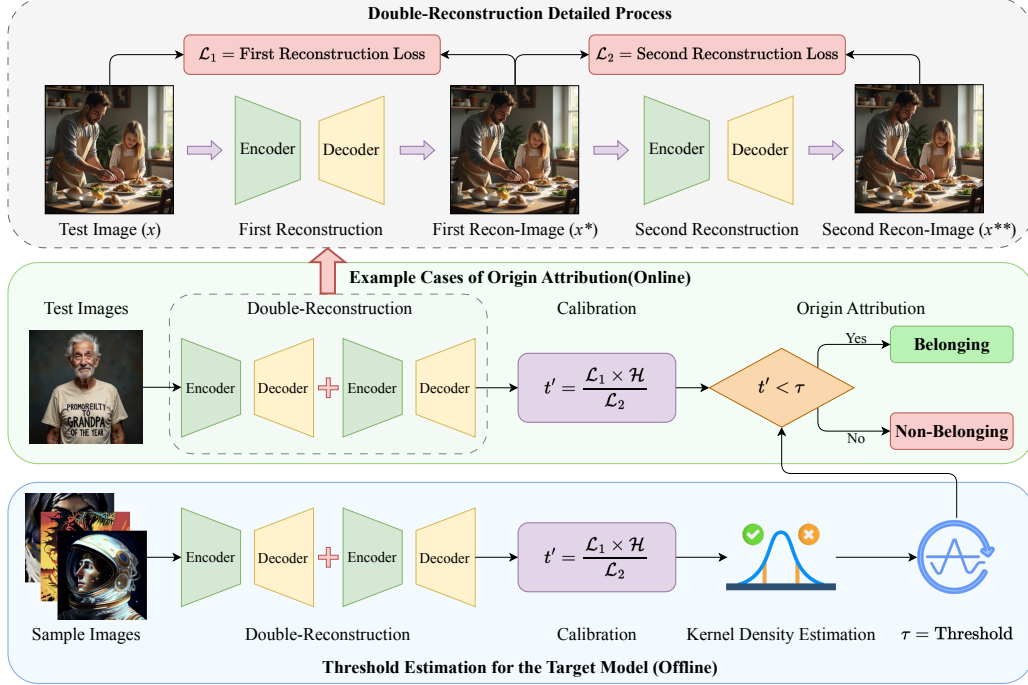


Figure 3: **The framework of AEDR.** Our method consists of three key modules: double-reconstruction based on autoencoder (4.2), calibration mechanism (4.3), and threshold determination via kernel density estimation (4.4). AEDR employs the ratio of double-reconstruction losses, calibrated by an image homogeneity metric, as the attribution signal. The decision threshold is determined via kernel density estimation and applied for origin attribution.

image  $x$  during the double-reconstruction process. Specifically, we define an uncalibrated attribution signal  $t$  as the ratio between the first and second reconstruction losses, formally given by:

$$t = \frac{\mathcal{L}_1}{\mathcal{L}_2} = \frac{\mathcal{L}(x^*, x)}{\mathcal{L}(x^{**}, x^*)}. \quad (3)$$

### 4.3 Calibration Mechanism

The inherent complexity of images significantly influences the reconstruction losses [26, 33, 47]. Images with homogeneous backgrounds and low texture complexity tend to exhibit minimal variations in double-reconstruction losses, while those with dynamic backgrounds and high-complexity textures demonstrate often lead to substantial loss fluctuations, refer to Appendix E. To mitigate this intrinsic complexity bias, we propose a homogeneity-aware loss calibration mechanism defined as:

$$\mathcal{H} = \sum_{i=0}^{l-1} \sum_{j=0}^{l-1} \frac{P(i, j)}{1 + |i - j|}, \quad (4)$$

where  $P(i, j)$  denotes the co-occurrence probability of grayscale levels  $i$  and  $j$  at a specified orientation and offset. The parameter  $l$  represents the total number of grayscale levels (default value of 32 to ensure computational efficiency), and  $|i - j|$  indicates the absolute difference in intensity between the corresponding pixel pairs. Based on this, the calibrated attribution signal is defined as follows:

$$t' = t \times \mathcal{H} = \frac{\mathcal{L}_1 \times \mathcal{H}}{\mathcal{L}_2}. \quad (5)$$

The calibrated metric  $t'$  effectively mitigates the intrinsic complexity bias in attribution assessment, thereby enhancing the overall attribution accuracy. Detailed experimental results, refer to Section 5.5.

#### 4.4 Threshold Determination via Kernel Density Estimation

Experimental results indicate that the calibrated attribution signal  $t'$  does not conform to any specific probability distribution across different models (see Appendix B) and may include a small number of outliers. To mitigate this, we employ the kernel density estimation (KDE) method [19], which makes no assumptions about the underlying distribution and is robust to outliers. The attribution threshold is determined using the cumulative distribution function (CDF) estimated from KDE, as formalized by:

$$\tau = \inf \left\{ u \mid \int_{-\infty}^u \frac{1}{N h} \sum_{i=1}^N K\left(\frac{y - t'_i}{h}\right) dy \geq 1 - \alpha \right\}, \quad (6)$$

where  $N$  (set to 500 in our experiments) denotes the number of samples. Specifically, 500 calibrated attribution signals from images attributed to the target model are used to estimate the distribution. The parameter  $h$  represents the bandwidth of the kernel density estimation [36], and  $K$  is the kernel function, for which a Gaussian kernel is used. The variable  $t'_i$  denotes the calibrated attribution signal of the  $i$ -th image. The quantity  $1 - \alpha$  represents the target cumulative probability.

If the calibrated attribution signal  $t' < \tau$ , the test image  $x$  is classified as a belonging image; otherwise, it is considered a non-belonging image. Experimental results indicate that the distribution of attribution signals varies across different generative models. Therefore, the key parameter  $\alpha$  must be determined according to the specific distributional characteristics of each model.

### 5 Experiments and Results

This section first outlines the experimental setup (Section 5.1). We then evaluate the effectiveness and efficiency of AEDR by comparing it with existing reconstruction-based approaches, namely RONAN [42] and LatentTracer [43] (Section 5.2 and Section 5.3). Furthermore, we analyze the generalization ability of AEDR across different autoencoder architectures (Section 5.4). Finally, we conduct ablation studies to validate the effectiveness of each component within AEDR (Section 5.5).

#### 5.1 Experimental Setup

**Models.** We evaluate AEDR on 8 text-to-image Latent Diffusion Models, including five variants of Stable Diffusion [35]: Stable Diffusion v1-5 (SD1.5), Stable Diffusion v2-base (SD2base), Stable Diffusion v2-1 (SD2.1), the higher-resolution Stable Diffusion XL-base-1.0 (SDXL), and the latest released Stable Diffusion 3.5-large (SD3.5). We also include FLUX.1-dev (FLUX) [22], based on rectified flows. All of these models employ Variational Autoencoders (VAE) [20], and we further consider two models built upon quantized autoencoders: Kandinsky 2.1 (KD2.1) [32], which uses the Modulating Quantized Vectors (MoVQ), and VQdiffusion (VQDM) [39], based on Vector Quantized Variational Autoencoder (VQ-VAE). For more details, refer to Appendix A.

**Dataset.** We construct a dataset consisting of 9,000 images, including 1,000 real images and 8,000 AI-generated images. The real images are randomly sampled from LAION-5B [37]. To reduce the influence of image diversity on experimental results, we employ the CLIP Interrogator [29] to extract prompts from the 1,000 real images. Each generative model then produces images based on these 1,000 prompts (see Appendix A). The first 500 generated images are used for hyperparameter tuning and threshold determination, while the remaining 500 are used for performance evaluation.

Our method is implemented using Python 3.10.17 and PyTorch 2.1.0. All experiments are conducted on an Ubuntu 18.04 server equipped with 8 NVIDIA RTX A6000 GPUs.

#### 5.2 Effectiveness

In this section, we evaluate the effectiveness of AEDR for origin attribution of AI-generated images from two perspectives: (1) distinguishing belonging images from those generated by other models; (2) distinguishing belonging images from real images.

**Distinguishing Belonging Images from Images Generated by Other Models.** We first evaluate the effectiveness of the proposed method in distinguishing belonging images from those generated by different models. We compare our method against existing reconstruction-based approaches, RO-

Table 1: Results for distinguishing belonging images and images generated by other models.

Model $\mathcal{M}_1$	Model $\mathcal{M}_2$	RONAN [42]					LatentTracer [43]					AEDR (ours)				
		TP	FP	TN	FN	Acc	TP	FP	TN	FN	Acc	TP	FP	TN	FN	Acc
SD1.5	SD2.1	476	475	24	25	50.1%	475	62	25	438	91.3%	493	13	7	487	<b>98.0%</b>
	SD2base	476	492	24	8	48.4%	475	41	25	459	93.4%	493	13	7	497	<b>98.0%</b>
	SD3.5	476	460	24	40	51.6%	475	43	25	457	93.2%	493	3	7	497	<b>99.0%</b>
	SDXL	476	491	24	9	48.5%	475	68	25	432	90.7%	493	10	7	490	<b>98.3%</b>
	FLUX	476	484	24	16	49.2%	475	78	25	422	89.7%	493	12	7	488	<b>98.1%</b>
	VQDM	476	499	24	1	47.7%	475	37	25	463	93.8%	493	5	7	495	<b>98.8%</b>
	KD2.1	476	471	24	29	50.5%	475	77	25	423	89.8%	493	4	7	496	<b>98.9%</b>
SD2.1	SD1.5	477	487	23	13	49.0%	476	244	24	256	73.2%	499	2	1	498	<b>99.7%</b>
	SD3.5	477	408	23	92	56.9%	476	288	24	212	68.8%	499	8	1	492	<b>99.1%</b>
	SDXL	477	500	23	0	47.7%	476	443	24	57	53.3%	499	1	1	499	<b>99.8%</b>
	FLUX	477	480	23	20	49.7%	476	409	24	91	56.7%	499	4	1	496	<b>99.5%</b>
	VQDM	477	499	23	1	47.8%	476	340	24	160	63.6%	499	0	1	500	<b>99.9%</b>
	KD2.1	477	495	23	5	48.2%	476	372	24	128	60.4%	499	1	1	499	<b>99.8%</b>
SD2base	SD1.5	475	409	25	91	56.6%	480	1	20	499	97.9%	499	11	1	489	<b>98.8%</b>
	SD3.5	475	387	25	113	58.8%	480	4	20	492	97.2%	499	14	1	486	<b>98.5%</b>
	SDXL	475	476	25	24	49.9%	480	9	20	491	97.1%	499	6	1	494	<b>99.3%</b>
	FLUX	475	460	25	40	51.5%	480	28	20	472	95.2%	499	17	1	483	<b>98.2%</b>
	VQDM	475	497	25	3	47.8%	480	5	20	495	97.5%	499	1	1	499	<b>99.8%</b>
	KD2.1	475	437	25	63	53.8%	480	30	20	470	95.0%	499	5	1	495	<b>99.4%</b>
SD3.5	SD1.5	479	500	21	0	47.9%	478	459	22	41	51.9%	490	7	10	493	<b>98.3%</b>
	SD2.1	479	499	21	1	48.0%	478	486	22	14	49.2%	490	11	10	489	<b>97.9%</b>
	SD2base	479	498	21	2	48.1%	478	489	22	11	48.9%	490	7	10	493	<b>98.3%</b>
	SDXL	479	499	21	1	48.0%	478	500	22	0	47.8%	490	42	10	458	<b>94.8%</b>
	FLUX	479	479	21	21	50.0%	478	500	22	0	47.8%	490	78	10	422	<b>91.2%</b>
	VQDM	479	499	21	1	48.0%	478	492	22	8	48.6%	490	2	10	498	<b>98.8%</b>
	KD2.1	479	467	21	33	51.2%	478	482	22	18	49.6%	490	22	10	478	<b>96.8%</b>
SDXL	SD1.5	474	468	26	32	50.6%	478	227	22	273	75.1%	500	5	0	495	<b>99.5%</b>
	SD2.1	474	469	26	31	50.5%	478	340	22	160	63.8%	500	3	0	497	<b>99.7%</b>
	SD2base	474	494	26	6	48.0%	478	295	22	205	68.3%	500	6	0	494	<b>99.4%</b>
	SD3.5	474	340	26	160	63.4%	478	292	22	208	68.6%	500	5	0	495	<b>99.5%</b>
	FLUX	474	442	26	58	53.2%	478	421	22	79	55.7%	500	15	0	485	<b>98.5%</b>
	VQDM	474	498	26	2	47.6%	478	349	22	151	62.9%	500	1	0	499	<b>99.9%</b>
	KD2.1	474	484	26	16	49.0%	478	364	22	136	61.4%	500	2	0	498	<b>99.8%</b>
FLUX	SD1.5	474	500	26	0	47.4%	478	407	22	93	57.1%	495	2	5	498	<b>99.3%</b>
	SD2.1	474	499	26	1	47.5%	478	434	22	66	54.4%	495	9	5	491	<b>98.6%</b>
	SD2base	474	497	26	3	47.7%	478	460	22	40	51.8%	495	6	5	494	<b>98.9%</b>
	SD3.5	474	472	26	28	50.2%	478	465	22	35	51.3%	495	41	5	459	<b>95.4%</b>
	SDXL	474	499	26	1	47.5%	478	476	22	24	50.2%	495	117	5	383	<b>87.8%</b>
	VQDM	474	305	26	195	66.9%	478	462	22	38	51.6%	495	1	5	499	<b>99.4%</b>
	KD2.1	474	469	26	31	50.5%	478	475	22	25	50.3%	495	27	5	473	<b>96.8%</b>
VQDM	SD1.5	476	487	24	13	48.9%	477	390	23	110	58.7%	469	105	31	395	<b>86.4%</b>
	SD2.1	476	472	24	28	50.4%	477	415	23	85	56.2%	469	94	31	406	<b>87.5%</b>
	SD2base	476	493	24	7	48.3%	477	402	23	98	57.5%	469	83	31	417	<b>88.6%</b>
	SD3.5	476	463	24	37	51.3%	477	446	23	54	53.1%	469	31	31	469	<b>93.8%</b>
	SDXL	476	490	24	10	48.6%	477	473	23	27	50.4%	469	50	31	450	<b>91.9%</b>
	FLUX	476	473	24	27	50.3%	477	481	23	19	49.6%	469	37	31	463	<b>93.2%</b>
	KD2.1	476	468	24	32	50.8%	477	421	23	79	55.6%	469	40	31	460	<b>92.9%</b>
KD2.1	SD1.5	481	483	19	17	49.8%	479	14	21	486	<b>96.5%</b>	472	157	28	343	81.5%
	SD2.1	481	487	19	13	49.4%	479	40	21	460	<b>93.9%</b>	472	215	28	285	75.7%
	SD2base	481	495	19	5	48.6%	479	24	21	476	<b>95.5%</b>	472	155	28	345	81.7%
	SD3.5	481	497	19	3	48.4%	479	36	21	464	<b>94.3%</b>	472	146	28	354	82.6%
	SDXL	481	493	19	7	48.8%	479	74	21	426	<b>90.5%</b>	472	188	28	312	78.4%
	FLUX	481	493	19	7	48.8%	479	82	21	418	<b>89.7%</b>	472	159	28	341	81.3%
	VQDM	481	497	19	3	48.4%	479	29	21	471	<b>95.0%</b>	472	50	28	450	92.2%
Avg Acc		50.3%					70.4%					<b>95.1%</b>				

NAN [42] and LatentTracer [43], to assess efficiency. All methods are tested on the same evaluation dataset in 8 models. For fair comparison, all baselines use official open source implementations.

The experimental results are shown in Table 1, where  $\mathcal{M}_1$  represents the target model and  $\mathcal{M}_2$  denotes other models. Our method achieves an average attribution accuracy of 95.1%, substantially outperforming RONAN and LatentTracer, which achieve 50.3% and 70.4%, respectively. While LatentTracer attains over 90% accuracy on models such as SD1.5, SD2base, and KD2.1, its performance degrades significantly on the remaining five models. The underlying reason is that when the target model is SD1.5, SD2base, and KD2.1, the reconstruction loss is on the order of  $10^{-3}$ , whereas for stronger models such as FLUX [22], the reconstruction loss decreases to approximately  $10^{-5}$  (see Figure 1 and Appendix F). And LatentTracer lacks any mechanism to calibrate the intrinsic complexity of images, resulting in substantial overlap between the distributions of belonging and non-belonging images, and thus a high false positive rate (FPR). These findings highlight the robust-

ness of AEDR, which improves attribution accuracy by 24.7% over the strongest baseline, particularly on state-of-the-art latent generative models.

**Distinguishing *Belonging Images* from *Real Images*.** We further assess the ability of AEDR to distinguish belonging images from real images. As shown in Table 2, AEDR achieves an average accuracy of 96.9%, significantly outperforming RONAN (52.2%) and LatentTracer (66.7%). These results confirm that AEDR offers a substantial advantage—30.2% improvement over the best baseline.

Table 2: Results for distinguishing belongings and real images.

Model	RONAN [42]					LatentTracer [43]					AEDR (ours)				
	TP	FP	TN	FN	Acc	TP	FP	TN	FN	Acc	TP	FP	TN	FN	Acc
SD1.5	476	481	24	19	49.5%	475	83	25	417	89.2%	493	6	7	494	<b>98.7%</b>
SD2.1	477	480	23	20	49.7%	476	417	24	83	55.9%	499	1	1	499	<b>99.8%</b>
SD2base	475	469	25	31	50.6%	480	29	20	471	95.1%	499	2	1	498	<b>99.7%</b>
SD3.5	479	393	21	107	58.6%	478	499	22	1	47.9%	490	15	10	485	<b>97.5%</b>
SDXL	474	479	26	21	49.5%	478	418	22	82	56.0%	500	3	0	497	<b>99.7%</b>
FLUX	474	370	26	130	60.4%	478	477	22	23	50.1%	495	25	5	475	<b>97.0%</b>
VQDM	476	473	24	27	50.3%	477	476	23	24	50.1%	469	44	31	456	<b>92.5%</b>
KD2.1	481	493	19	7	48.8%	479	83	21	417	89.6%	472	72	28	428	<b>90.0%</b>
Avg Acc	52.2%					66.7%					<b>96.9%</b>				

### 5.3 Efficiency

In this section, we evaluate the computational efficiency of our method. We test all 8 models with 1,000 images each, recording the average runtime for comparison. Due to memory constraints, we use bf16 precision for FLUX [22] and SD3.5 [13], while the remaining six models are run with fp32 precision. LatentTracer [43] initializes gradient optimization using encoded representations of the input images, while RONAN [42] uses random initialization and thus requires more optimization steps. Hence, our comparison focuses on LatentTracer as the more efficient baseline. As shown in Table 3, AEDR achieves a remarkable improvement in runtime efficiency, requiring only 1% of the runtime of LatentTracer [43]. This gain is primarily attributed to AEDR’s design, which replaces iterative gradient-based optimization with two simple forward passes through the autoencoder.

Table 3: Runtime on different models.

Model	LatentTracer [43]	AEDR (ours)
SD1.5	29.85s	<b>0.27s</b>
SD2.1	92.09s	<b>0.62s</b>
SD2base	32.89s	<b>0.25s</b>
SD3.5	29.85s	<b>0.69s</b>
SDXL	162.94s	<b>1.25s</b>
FLUX	30.64s	<b>0.68s</b>
VQDM	12.58s	<b>0.06s</b>
KD2.1	48.14s	<b>0.39s</b>

Table 4: Generalization to different types of AE.

AE Type	Model	RONAN [42]	LatentTracer [43]	AEDR (ours)
VAE	SD1.5	49.44%	91.39%	<b>98.45%</b>
VAE	SD2.1	49.86%	61.70%	<b>99.66%</b>
VAE	SD2base	52.71%	96.43%	<b>99.10%</b>
VAE	SD3.5	49.98%	48.96%	<b>96.70%</b>
VAE	SDXL	51.48%	63.98%	<b>99.50%</b>
VAE	FLUX	52.26%	52.10%	<b>96.65%</b>
VQ-VAE	VQDM	49.86%	54.44%	<b>90.85%</b>
MoVQ	KD2.1	48.88%	<b>93.13%</b>	82.93%

### 5.4 Generalization Across Autoencoder Architectures

We evaluate the generalization capability of AEDR across three distinct autoencoder architectures: VAE [20], VQ-VAE [39, 41], and MoVQ [32, 52]. As shown in Figure 4, AEDR achieves an attribution accuracy exceeding 96% on VAE-based models. On VQ-VAE, the accuracy reaches 90.85%, and on MoVQ, it attains 82.93%. The performance degradation is mainly due to the fact that the latent space of the quantized model is discrete. The input tensor is quantized to the nearest latent code, and this quantization error makes it difficult to achieve fine-grained reconstruction. Nonetheless, AEDR outperforms LatentTracer [43] on VQ-VAE, while MoVQ remains challenging, highlighting an avenue for future work.

### 5.5 Ablation Studies

**Impact of Reconstruction Loss Metric.** We evaluate the effect of different reconstruction loss metrics on attribution accuracy using the SD2.1. Four commonly used metrics are compared: Mean Absolute Error (MAE), Mean Squared Error (MSE), Structural Similarity Index (SSIM), and Learned



Table 5: Results on different loss metrics.

Metric	TP	FP	FN	TN	Acc
MAE	497	25	3	475	97.20%
MSE	<b>496</b>	<b>2</b>	<b>4</b>	<b>498</b>	<b>99.40%</b>
SSIM	495	4	5	496	99.10%
LPIPS	494	87	6	413	90.70%

Table 6: Effects of homogeneity calibration.

Model	w/o Calibration	w/ Calibration	Improvement
SD1.5	96.29%	<b>98.45%</b>	+2.16%
SD2.1	90.57%	<b>99.66%</b>	+9.09%
SD2base	93.71%	<b>99.10%</b>	+5.39%
SD3.5	94.97%	<b>96.70%</b>	+1.73%
SDXL	99.32%	<b>99.50%</b>	+0.18%
FLUX	<b>96.80%</b>	96.65%	-0.15%
VQDM	<b>92.80%</b>	90.85%	-1.95%
KD2.1	78.35%	<b>82.93%</b>	+4.58%

Perceptual Image Patch Similarity (LPIPS) [6, 34]. As shown in Table 5, the attribution accuracies are 97.20% (MAE), 99.40% (MSE), 99.10% (SSIM), and 90.70% (LPIPS), respectively. Therefore, we adopt MSE as the default reconstruction loss metric in AEDR.

**Impact of Homogeneity Calibration.** This section examines the impact of incorporating image homogeneity [10] to reduce the effect of inherent image complexity on attribution accuracy. As shown in Table 6, based on homogeneity calibration, most models achieve significant performance improvements, with gains ranging from 0.18% to 9.09%, whereas FLUX and VQDM exhibit decreases in attribution accuracy of 0.15% and 1.95%. While some models exhibit marginal performance declines, the overall benefit brought by the calibration mechanism outweighs these drawbacks.

**Impact of Quantile Selection.** This section investigates how different quantile selections affect attribution accuracy. Due to the significant variation in the distribution of attribution signals across models (see Appendix B), we select model-specific quantile parameters. Each model is tested with 1,000 belonging images: 500 are used for threshold estimation, and the remaining 500 for evaluation. For each model, we select the value of  $\alpha$  that yields the highest average accuracy across both subsets as the final quantile. The selected  $\alpha$  values are summarized in Table 7. More details in Appendix B.

Table 7: The Selection of Quantile.

Model	$\alpha$	Estimation	Evaluation	Avg Acc	Model	$\alpha$	Estimation	Evaluation	Avg Acc
SD1.5	0.01	98.64%	98.30%	98.47%	SDXL	0.002	99.10%	99.49%	99.30%
	<b>0.015</b>	<b>98.67%</b>	<b>98.48%</b>	<b>98.58%</b>		<b>0.003</b>	<b>99.25%</b>	<b>99.50%</b>	<b>99.38%</b>
	0.02	98.28%	98.53%	98.41%		0.004	99.19%	99.41%	99.30%
SD2.1	0.002	99.67%	99.69%	99.68%	FLUX	0.015	96.24%	96.57%	96.41%
	<b>0.003</b>	<b>99.73%</b>	<b>99.66%</b>	<b>99.70%</b>		<b>0.02</b>	<b>96.28%</b>	<b>96.65%</b>	<b>96.47%</b>
	0.004	99.64%	99.67%	99.66%		0.025	96.10%	96.69%	96.40%
SD2base	0.004	99.07%	99.00%	99.04%	VQDM	0.08	90.47%	90.61%	90.54%
	<b>0.005</b>	<b>99.04%</b>	<b>99.10%</b>	<b>99.07%</b>		<b>0.085</b>	<b>90.38%</b>	<b>90.85%</b>	<b>90.62%</b>
	0.006	99.14%	98.96%	99.05%		0.09	90.29%	90.81%	90.55%
SD3.5	0.03	96.01%	96.43%	96.22%	KD2.1	0.045	83.35%	82.51%	82.93%
	<b>0.035</b>	<b>96.15%</b>	<b>96.70%</b>	<b>96.43%</b>		<b>0.05</b>	<b>83.47%</b>	<b>82.93%</b>	<b>83.20%</b>
	0.04	95.76%	96.77%	96.27%		0.055	83.41%	82.79%	83.10%

## 6 Limitations

Although our method achieves high attribution accuracy and computational efficiency for image generation models based on continuous autoencoders [20], its performance degrades when applied to models utilizing quantized autoencoders [41, 52]. This limitation reduces the generalization ability of ADER in broader application scenarios. Another limitation of our method lies in its inability to distinguish between images generated by different models that share an identical autoencoder, such as Stable Diffusion v2-1 and Stable Diffusion v2-base. However, as image generation models continue to evolve rapidly, it is increasingly common for developers to fine-tune autoencoders during training to better suit specific model architectures.

## 7 Conclusion

In this paper, we address the critical challenges encountered by current reconstruction-based attribution methods when dealing with SOTA generative models. We propose AEDR, a novel AI-generated image attribution approach that integrates double autoencoder reconstruction with an effective calibration mechanism based on image homogeneity. By computing the reconstruction loss ratio over two consecutive reconstructions, AEDR efficiently mitigates biases introduced by varying image complexities, resulting in significantly improved attribution performance. Extensive experiments confirm that AEDR achieves a relative improvement of 25.5% in attribution accuracy, while simultaneously reducing inference time to only 1% of that required by the leading baseline methods.

## References

- [1] James Betker, Gabriel Goh, Li Jing, Tim Brooks, Jianfeng Wang, Linjie Li, Long Ouyang, Juntang Zhuang, Joyce Lee, Yufei Guo, et al. Improving image generation with better captions. *Computer Science*. <https://cdn.openai.com/papers/dall-e-3.pdf>, 2(3):8, 2023.
- [2] Nicolas Carlini, Jamie Hayes, Milad Nasr, Matthew Jagielski, Vikash Sehwal, Florian Tramer, Borja Balle, Daphne Ippolito, and Eric Wallace. Extracting training data from diffusion models. In *32nd USENIX Security Symposium (USENIX Security 23)*, pages 5253–5270, 2023.
- [3] Chen Chen, Jie Fu, and Lingjuan Lyu. A pathway towards responsible ai generated content. *arXiv preprint arXiv:2303.01325*, 2023.
- [4] Dingfan Chen, Ning Yu, Yang Zhang, and Mario Fritz. Gan-leaks: A taxonomy of membership inference attacks against generative models. In *Proceedings of the 2020 ACM SIGSAC conference on computer and communications security*, pages 343–362, 2020.
- [5] Yuming Chen and Maryam Yashtini. Detecting ai generated images through texture and frequency analysis of patches. In *2024 4th International Conference on Artificial Intelligence, Virtual Reality and Visualization*, pages 103–110. IEEE, 2024.
- [6] Sungik Choi, Sungwoo Park, Jaehoon Lee, Seunghyun Kim, Stanley Jungkyu Choi, and Moontae Lee. Hfi: A unified framework for training-free detection and implicit watermarking of latent diffusion model generated images. *arXiv preprint arXiv:2412.20704*, 2024.
- [7] Riccardo Corvi, Davide Cozzolino, Giovanni Poggi, Koki Nagano, and Luisa Verdoliva. Intriguing properties of synthetic images: from generative adversarial networks to diffusion models. In *Proceedings of the IEEE/CVF conference on computer vision and pattern recognition*, pages 973–982, 2023.
- [8] Prafulla Dhariwal and Alexander Nichol. Diffusion models beat gans on image synthesis. *Advances in neural information processing systems*, 34:8780–8794, 2021.
- [9] Yuzhen Ding, Nupur Thakur, and Baoxin Li. Does a gan leave distinct model-specific fingerprints? In *BMVC*, page 22, 2021.
- [10] Melanie Dohmen, Mark A Klemens, Ivo M Baltruschat, Tuan Truong, and Matthias Lenga. Similarity and quality metrics for mr image-to-image translation. *arXiv preprint arXiv:2405.08431*, 2024.
- [11] Chengdong Dong, Ajay Kumar, and Eryun Liu. Think twice before detecting gan-generated fake images from their spectral domain imprints. In *Proceedings of the IEEE/CVF conference on computer vision and pattern recognition*, pages 7865–7874, 2022.
- [12] Tarik Dzanic, Karan Shah, and Freddie Witherden. Fourier spectrum discrepancies in deep network generated images. *Advances in neural information processing systems*, 33:3022–3032, 2020.
- [13] Patrick Esser, Sumith Kulal, Andreas Blattmann, Rahim Entezari, Jonas Müller, Harry Saini, Yam Levi, Dominik Lorenz, Axel Sauer, Frederic Boesel, et al. Scaling rectified flow transformers for high-resolution image synthesis. In *Forty-first international conference on machine learning*, 2024.
- [14] Joel Frank, Thorsten Eisenhofer, Lea Schönherr, Asja Fischer, Dorothea Kolossa, and Thorsten Holz. Leveraging frequency analysis for deep fake image recognition. In *International conference on machine learning*, pages 3247–3258. PMLR, 2020.
- [15] Ian J Goodfellow, Jean Pouget-Abadie, Mehdi Mirza, Bing Xu, David Warde-Farley, Sherjil Ozair, Aaron Courville, and Yoshua Bengio. Generative adversarial nets. *Advances in neural information processing systems*, 27, 2014.
- [16] Seoyeon Gye, Junwon Ko, Hyounguk Shon, Minchan Kwon, and Junmo Kim. Reducing the content bias for ai-generated image detection. In *2025 IEEE/CVF Winter Conference on Applications of Computer Vision (WACV)*, pages 399–408. IEEE, 2025.
- [17] Jonathan Ho, Ajay Jain, and Pieter Abbeel. Denoising diffusion probabilistic models. *Advances in neural information processing systems*, 33:6840–6851, 2020.
- [18] Yonghyun Jeong, Doyeon Kim, Seungjai Min, Seongho Joe, Youngjune Gwon, and Jongwon Choi. Bihpf: Bilateral high-pass filters for robust deepfake detection. In *Proceedings of the IEEE/CVF Winter Conference on Applications of Computer Vision*, pages 48–57, 2022.
- [19] JooSeuk Kim and Clayton D Scott. Robust kernel density estimation. *The Journal of Machine Learning Research*, 13(1):2529–2565, 2012.

- [20] Diederik P. Kingma and Max Welling. Auto-encoding variational bayes. In Yoshua Bengio and Yann LeCun, editors, *2nd International Conference on Learning Representations, ICLR 2014, Banff, AB, Canada, April 14-16, 2014, Conference Track Proceedings*, 2014.
- [21] Despina Konstantinidou, Christos Koutlis, and Symeon Papadopoulos. Texturecrop: Enhancing synthetic image detection through texture-based cropping. In *Proceedings of the Winter Conference on Applications of Computer Vision*, pages 1459–1468, 2025.
- [22] Black Forest Labs. Flux. <https://github.com/black-forest-labs/flux>, 2024.
- [23] Boheng Li, Yanhao Wei, Yankai Fu, Zhenting Wang, Yiming Li, Jie Zhang, Run Wang, and Tianwei Zhang. Towards reliable verification of unauthorized data usage in personalized text-to-image diffusion models. *arXiv preprint arXiv:2410.10437*, 2024.
- [24] Jun Li, Wentao Jiang, Liyan Shen, and Yawei Ren. Optimized frequency collaborative strategy drives ai image detection. *IEEE Internet of Things Journal*, 2025.
- [25] Lixin Luo, Zhenyong Chen, Ming Chen, Xiao Zeng, and Zhang Xiong. Reversible image watermarking using interpolation technique. *IEEE Transactions on information forensics and security*, 5(1):187–193, 2009.
- [26] I Mario, M Chacon, D Alma, and S Corral. Image complexity measure: a human criterion free approach. In *NAFIPS 2005-2005 Annual Meeting of the North American Fuzzy Information Processing Society*, pages 241–246. IEEE, 2005.
- [27] Ding Sheng Ong, Chee Seng Chan, Kam Woh Ng, Lixin Fan, and Qiang Yang. Protecting intellectual property of generative adversarial networks from ambiguity attacks. In *Proceedings of the IEEE/CVF Conference on Computer Vision and Pattern Recognition*, pages 3630–3639, 2021.
- [28] Shelby Pereira and Thierry Pun. Robust template matching for affine resistant image watermarks. *IEEE transactions on image Processing*, 9(6):1123–1129, 2000.
- [29] Pharmapsychotic. Clip-interrogator. <https://github.com/pharmapsychotic/clip-interrogator>, 2023.
- [30] Dustin Podell, Zion English, Kyle Lacey, Andreas Blattmann, Tim Dockhorn, Jonas Müller, Joe Penna, and Robin Rombach. Sdxl: Improving latent diffusion models for high-resolution image synthesis. *arXiv preprint arXiv:2307.01952*, 2023.
- [31] Syed Ali Raza, Usman Habib, Muhammad Usman, Adeel Ashraf Cheema, and Muhammad Sajid Khan. Mmganguard: a robust approach for detecting fake images generated by gans using multi-model techniques. *IEEE Access*, 2024.
- [32] Anton Razzhigaev, Arseniy Shakhmatov, Anastasia Maltseva, Vladimir Arkhipkin, Igor Pavlov, Ilya Ryabov, Angelina Kuts, Alexander Panchenko, Andrey Kuznetsov, and Denis Dimitrov. Kandinsky: an improved text-to-image synthesis with image prior and latent diffusion. *arXiv preprint arXiv:2310.03502*, 2023.
- [33] Christoph Redies, Seyed Ali Amirshahi, Michael Koch, and Joachim Denzler. Phog-derived aesthetic measures applied to color photographs of artworks, natural scenes and objects. In *European conference on computer vision*, pages 522–531. Springer, 2012.
- [34] Jonas Ricker, Denis Lukovnikov, and Asja Fischer. Aeroblade: Training-free detection of latent diffusion images using autoencoder reconstruction error. In *Proceedings of the IEEE/CVF Conference on Computer Vision and Pattern Recognition*, pages 9130–9140, 2024.
- [35] Robin Rombach, Andreas Blattmann, Dominik Lorenz, Patrick Esser, and Björn Ommer. High-resolution image synthesis with latent diffusion models. In *Proceedings of the IEEE/CVF conference on computer vision and pattern recognition*, pages 10684–10695, 2022.
- [36] Warangkana Ruckthongsook, Chetan Tiwari, Joseph R Oppong, and Prathiba Natesan. Evaluation of threshold selection methods for adaptive kernel density estimation in disease mapping. *International Journal of Health Geographics*, 17:1–13, 2018.
- [37] Christoph Schuhmann, Romain Beaumont, Richard Vencu, Cade Gordon, Ross Wightman, Mehdi Cherti, Theo Coombes, Aarush Katta, Clayton Mullis, Mitchell Wortsman, et al. Laion-5b: An open large-scale dataset for training next generation image-text models. *Advances in neural information processing systems*, 35: 25278–25294, 2022.
- [38] Mitchell D Swanson, Bin Zhu, and Ahmed H Tewfik. Transparent robust image watermarking. In *Proceedings of 3rd IEEE International Conference on Image Processing*, volume 3, pages 211–214. IEEE, 1996.

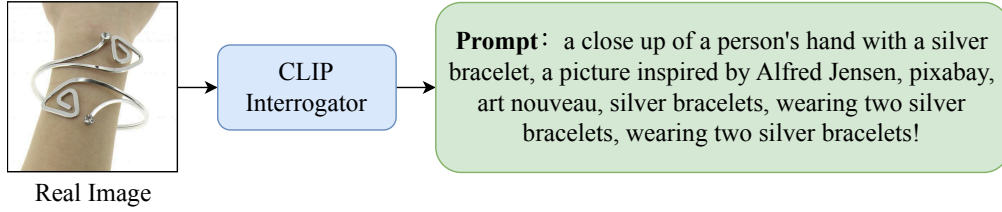
- [39] Zhicong Tang, Shuyang Gu, Jianmin Bao, Dong Chen, and Fang Wen. Improved vector quantized diffusion models. *arXiv preprint arXiv:2205.16007*, 2022.
- [40] Aäron Van Den Oord, Nal Kalchbrenner, and Koray Kavukcuoglu. Pixel recurrent neural networks. In *International conference on machine learning*, pages 1747–1756. PMLR, 2016.
- [41] Aaron Van Den Oord, Oriol Vinyals, et al. Neural discrete representation learning. *Advances in neural information processing systems*, 30, 2017.
- [42] Zhenting Wang, Chen Chen, Yi Zeng, Lingjuan Lyu, and Shiqing Ma. Where did i come from? origin attribution of ai-generated images. In *Thirty-seventh Conference on Neural Information Processing Systems*, 2023.
- [43] Zhenting Wang, Chen Sehwas Vikash, Chen, Lingjuan Lyu, Dimitris N Metaxas, and Shiqing Ma. How to trace latent generative model generated images without artificial watermark? In *International Conference on Machine Learning*, 2024.
- [44] Yuxin Wen, John Kirchenbauer, Jonas Geiping, and Tom Goldstein. Tree-ring watermarks: Fingerprints for diffusion images that are invisible and robust. *arXiv preprint arXiv:2305.20030*, 2023.
- [45] Zijin Yang, Kai Zeng, Kejiang Chen, Han Fang, Weiming Zhang, and Nenghai Yu. Gaussian shading: Provable performance-lossless image watermarking for diffusion models. In *Proceedings of the IEEE/CVF Conference on Computer Vision and Pattern Recognition*, pages 12162–12171, 2024.
- [46] Zijin Yang, Xin Zhang, Kejiang Chen, Kai Zeng, Qiyi Yao, Han Fang, Weiming Zhang, and Nenghai Yu. Gaussian shading++: Rethinking the realistic deployment challenge of performance-lossless image watermark for diffusion models. *arXiv preprint arXiv:2504.15026*, 2025.
- [47] Honghai Yu and Stefan Winkler. Image complexity and spatial information. In *2013 Fifth International Workshop on Quality of Multimedia Experience (QoMEX)*, pages 12–17. IEEE, 2013.
- [48] Ning Yu, Larry S Davis, and Mario Fritz. Attributing fake images to gans: Learning and analyzing gan fingerprints. In *Proceedings of the IEEE/CVF international conference on computer vision*, pages 7556–7566, 2019.
- [49] Ning Yu, Vladislav Skripniuk, Dingfan Chen, Larry Davis, and Mario Fritz. Responsible disclosure of generative models using scalable fingerprinting. *arXiv preprint arXiv:2012.08726*, 2020.
- [50] Ning Yu, Vladislav Skripniuk, Sahar Abdelnabi, and Mario Fritz. Artificial fingerprinting for generative models: Rooting deepfake attribution in training data. In *Proceedings of the IEEE/CVF International conference on computer vision*, pages 14448–14457, 2021.
- [51] Hanqing Zhao, Wenbo Zhou, Dongdong Chen, Tianyi Wei, Weiming Zhang, and Nenghai Yu. Multi-attentional deepfake detection. In *Proceedings of the IEEE/CVF conference on computer vision and pattern recognition*, pages 2185–2194, 2021.
- [52] Chuanxia Zheng, Tung-Long Vuong, Jianfei Cai, and Dinh Phung. Movq: Modulating quantized vectors for high-fidelity image generation. *Advances in Neural Information Processing Systems*, 35:23412–23425, 2022.

## A More Details of the Used Models and Images

In this section, we provide a detailed description of the models and specific parameters used in the experiments. We also present the image generation resolutions and the corresponding types of autoencoders used in each model. More details are shown in Table 8. We then demonstrate the process of extracting prompts from real images using the CLIP Interrogator, followed by generating corresponding images with the eight models described above, as illustrated in Figure 4. Our dataset is constructed based on the parameters and procedures described above, consisting of 1,000 real images and 8,000 AI-generated images. Half of the dataset is used for threshold determination and the other half is used for performance evaluation.

Table 8: Detailed settings of the models in the experiment.

Model	Type of AE	Image size	Num inference steps	Guidance scale
Stable Diffusion v1-5	VAE	$512 \times 512$	80	7.5
Stable Diffusion v2-1	VAE	$768 \times 768$	80	7.5
Stable Diffusion v2-base	VAE	$512 \times 512$	80	7.5
Stable Diffusion 3.5-large	VAE	$1024 \times 1024$	35	7.5
Stable Diffusion XL-base-1.0	VAE	$1024 \times 1024$	80	7.5
FLUX.1-dev	VAE	$1024 \times 1024$	35	7.5
VQdiffusion	VQ-VAE	$256 \times 256$	80	7.5
Kandinsky 2.1	MoVQ	$512 \times 512$	80	7.5



(a) Extracting prompt from real image using the CLIP Interrogator.



(b) Generate images using models and the same prompt in (a).

Figure 4: Prompt extraction from real images and AI-generated image demonstration.

## B More Details of Quantile Selection

Due to space constraints, Section 5.5 only presents the selected quantiles for different models. Since different models exhibit varying distributions of the attribution signal  $t'$ , as shown in Figure 5, we provide a detailed analysis in this section of how different quantile selections affect attribution accuracy. For each model, 4,500 images are used for threshold estimation and another 4,500 images for evaluation, resulting in a total of 9,000 images, including both real images and images generated by the eight models. The final threshold for each model is determined based on the quantile that achieves the highest average attribution accuracy. Detailed experimental results are presented in Table 9, with the best-performing results highlighted in bold.

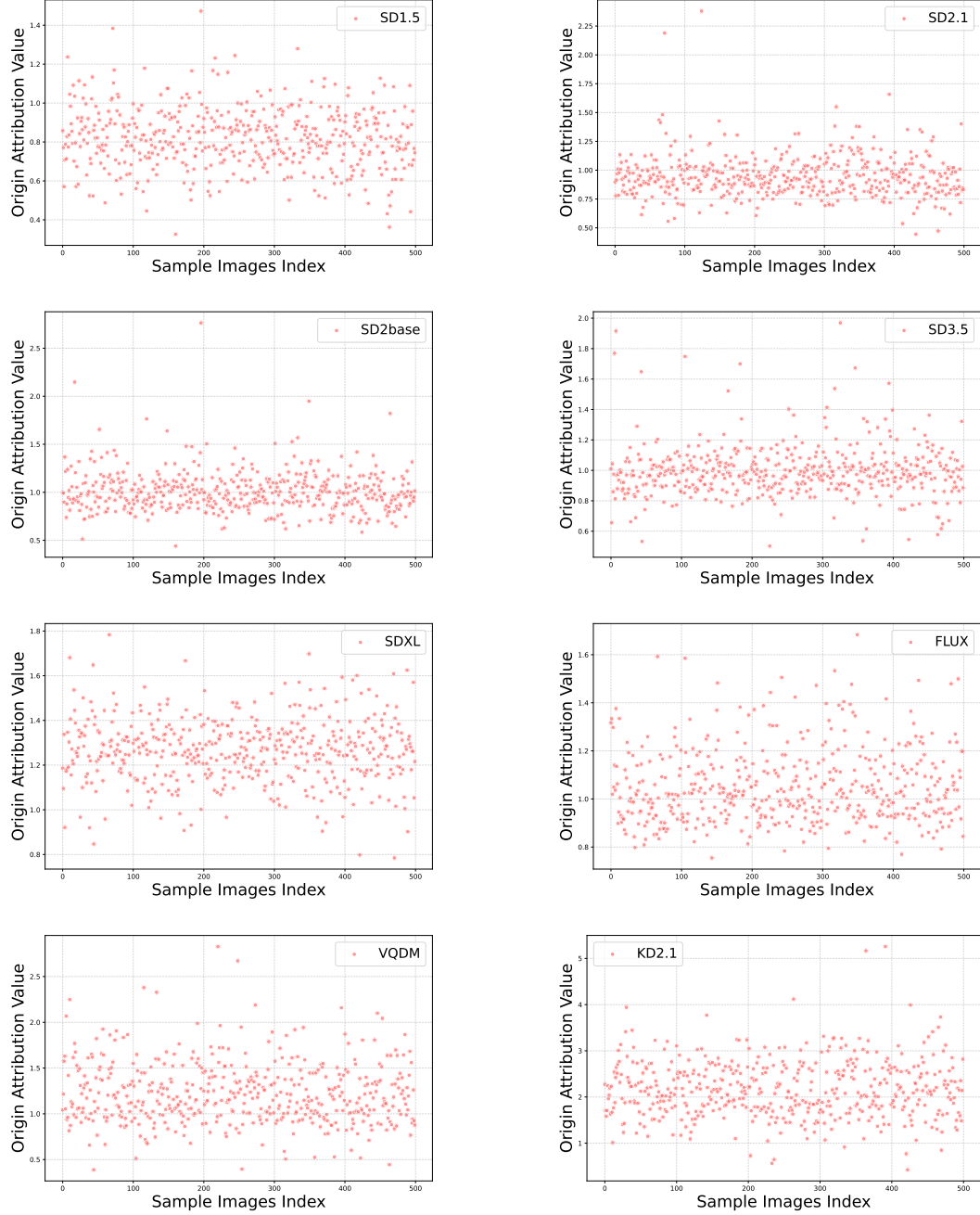


Figure 5: Different models exhibit varying distributions of the origin attribution signal.

Table 9: The impact of different quantile selections on attribution accuracy.

Model	Alpha	Estimation Acc	Evaluation Acc	Avg Acc	Model	Alpha	Estimation Acc	Evaluation Acc	Avg Acc
SD1.5	0.01	98.64%	98.30%	98.47%	SDXL	0.001	98.85%	99.49%	99.17%
	<b>0.015</b>	<b>98.67%</b>	<b>98.48%</b>	<b>98.58%</b>		0.002	99.10%	99.49%	99.30%
	0.02	98.28%	98.53%	98.41%		<b>0.003</b>	<b>99.25%</b>	<b>99.50%</b>	<b>99.38%</b>
	0.025	97.99%	98.32%	98.16%		0.004	99.19%	99.41%	99.30%
	0.03	97.88%	98.16%	98.02%		0.005	99.24%	99.42%	99.33%
	0.035	97.84%	97.70%	97.77%		0.006	99.29%	99.44%	99.37%
SD2.1	0.002	99.67%	99.69%	99.68%	FLUX	0.01	96.15%	96.39%	96.27%
	<b>0.003</b>	<b>99.73%</b>	<b>99.66%</b>	<b>99.70%</b>		0.015	96.24%	96.57%	96.41%
	0.004	99.64%	99.67%	99.66%		<b>0.02</b>	<b>96.28%</b>	<b>96.65%</b>	<b>96.47%</b>
	0.005	99.64%	99.57%	99.61%		0.025	96.10%	96.69%	96.40%
	0.01	99.44%	99.50%	99.47%		0.03	96.14%	96.39%	96.27%
	0.015	99.26%	99.30%	99.28%		0.035	96.12%	96.12%	96.12%
SD2base	0.003	99.09%	98.94%	99.02%	VQDM	0.075	90.33%	90.70%	90.52%
	0.004	99.07%	99.00%	99.04%		0.08	90.47%	90.61%	90.54%
	<b>0.005</b>	<b>99.04%</b>	<b>99.10%</b>	<b>99.07%</b>		<b>0.085</b>	<b>90.38%</b>	<b>90.85%</b>	<b>90.62%</b>
	0.008	99.14%	98.96%	99.05%		0.09	90.29%	90.81%	90.55%
	0.009	99.20%	98.90%	99.05%		0.095	90.31%	90.89%	90.60%
	0.01	99.16%	98.90%	99.03%		0.1	90.41%	90.72%	90.57%
SD3.5	0.025	95.88%	96.21%	96.05%	KD2.1	0.03	82.64%	81.55%	82.10%
	0.03	96.01%	96.43%	96.22%		0.035	82.88%	81.95%	82.42%
	<b>0.035</b>	<b>96.15%</b>	<b>96.70%</b>	<b>96.43%</b>		0.04	83.19%	82.24%	82.72%
	0.04	95.76%	96.77%	96.27%		0.045	83.35%	82.51%	82.93%
	0.045	95.94%	96.75%	96.35%		<b>0.05</b>	<b>83.47%</b>	<b>82.93%</b>	<b>83.20%</b>
	0.05	95.76%	96.88%	96.32%		0.055	83.41%	82.79%	83.10%

Experimental results show that different models require different quantile selections. As the  $\alpha$  value increases from zero, the attribution accuracy first increases and then decreases, reaching its maximum at the optimal quantile. In practical deployment, model owners can continuously expand the number of sample images to compute a more precise and model-specific attribution threshold. In addition, the attribution strength can be adjusted according to the requirements of different application scenarios.

## C Reasons and Advantages of Double-Reconstruction

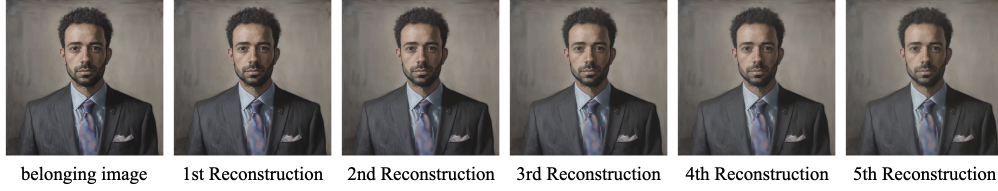
In this section, we explain the rationale behind selecting the Double-Reconstruction strategy and highlight its advantages. We first present the loss variation over five consecutive reconstructions on the same image (both belonging and non-belonging images) using the Stable Diffusion XL-base-1.0 model, as shown in Figure 6 and Table 10. In this experiment, the image under test is used as the input for the first reconstruction, and subsequent reconstructions use the image from the previous reconstruction as the input. The computed loss values are based on the input and output images from each reconstruction, rather than being calculated in reference to the original image. At the same time, we also compared it with the cumulative loss to show the superiority of single loss change.

Table 10: Loss for five consecutive reconstructions of belonging and non-belonging images.

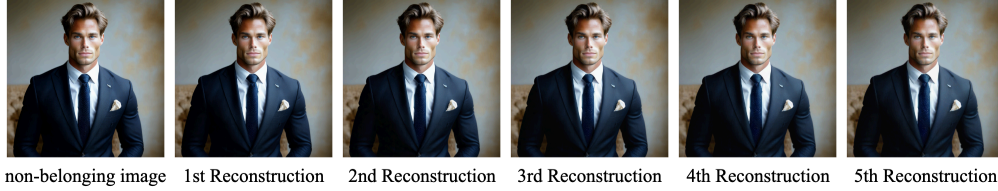
Reconstruction Times	Belong Image		Non-Belong Image	
	Single Loss	Cumulative Loss	Single Loss	Cumulative Loss
First Reconstruction	<b>0.00030581</b>	0.00030581	<b>0.00164355</b>	0.00164355
Second Reconstruction	<b>0.00021323</b>	0.00067133	<b>0.00046879</b>	0.00200841
Third Reconstruction	<b>0.00018301</b>	0.00110267	<b>0.00033344</b>	0.00253991
Fourth Reconstruction	<b>0.00016603</b>	0.00160316	<b>0.00029531</b>	0.00322278
Fifth Reconstruction	<b>0.00016056</b>	0.00215988	<b>0.00025636</b>	0.00401155

The experimental results show that in both the first and second reconstructions, belonging images are reconstructed in a similar fashion, with their reconstruction losses remaining nearly identical. By contrast, non-belonging images incur a much larger loss on the first pass; after this first reconstruction, such an image is effectively projected onto the distribution learned by the autoencoder, resulting in a marked decrease in the second reconstruction loss. Accordingly, we define the attribution signal as the ratio of the first reconstruction loss to the second, which not only inherently removes any absolute





(a) Five consecutive reconstructions of the belonging image.



(b) Five consecutive reconstructions of the non-belonging image.

Figure 6: (a) and (b) show the five consecutive reconstruction processes of the belonging image and the non-belonging image. We found that in each reconstruction process, the reconstruction effect of the details is not good, such as the corners of the eyes and the scarf in the silk pocket.

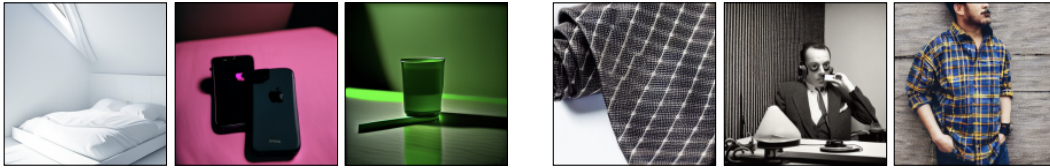
offset caused by differences in image complexity but also robustly discriminates between belonging and non-belonging images.

## D Two Core Theoretical Insights of AEDR

**Attribution Principle.** Due to the stochastic sampling process inherent in continuous autoencoders, the latent vectors corresponding to images generated by the model  $M$  typically lie in high-probability regions of the autoencoder’s internal feature distribution. Although minor reconstruction errors may occur due to sampling randomness, such errors remain within an acceptable range for the autoencoder, resulting in relatively stable reconstruction losses across a double-reconstruction process.

**Attribution vs. Non-attribution Discrimination.** For non-belonging images, the latent vector obtained during the initial reconstruction tends to deviate significantly from the learned distribution of autoencoder, leading to a higher reconstruction loss. However, after the first reconstruction(that is, feeding the first reconstructed output into the autoencoder a second time), the second output becomes better aligned with the internal feature distribution, causing a notable reduction in the second reconstruction loss. This results in a large difference between the two reconstruction losses, which serves as a discriminative signal.

## E Two Types of Attribution Errors



(a) Non-Belonging Images with Small Loss Variation

(b) Belonging Images with Large Loss Variation

Figure 7: (a) and (b) respectively illustrate two types of attribution errors. The target model used for evaluation is Stable Diffusion v1-5. The test set consists of 500 images generated by Stable Diffusion v1-5 (Belonging) and 500 images generated by Kandinsky 2.1 (Non-Belonging).

Figure 7 presents two types of misattributed samples: false positives (non-belonging images identified as belonging) and false negatives (belonging images identified as non-belonging). We observe

that images with low reconstruction loss ratio tend to have simple, homogeneous backgrounds and limited detail, while those with high ratios often contain complex textures and rich visual content. These examples illustrate a known limitation of autoencoder-based reconstructions in preserving fine-grained details [6, 34], highlighting the necessity of incorporating a loss calibration mechanism.

## F Loss Characteristics based on Gradient Reconstruction

With the rapid advancement of image generation models, gradient-based reconstructions have become nearly indistinguishable from the original images, resulting in extremely low reconstruction losses. Consequently, slight variations caused by inherent image complexity can lead to significant overlap in the loss distributions of attributed and non-attributed images, hindering precise attribution. The Figure 8 and Table 11 illustrate this issue using four test images and their reconstruction losses across eight different generative models.



Figure 8: 4 sample images for gradient reconstruction.

Table 11: Loss of gradient-based reconstruction.

Model	reconstruction loss			
	Image-1	Image-2	Image-3	Image-4
SD1.5	0.00021821	0.00071571	0.00151912	0.00012126
SD2.1	0.00004312	0.00018105	0.00034466	0.00003273
SD2base	0.00017373	0.00067367	0.00143998	0.00010398
SD3.5	0.00008450	0.00011302	0.00013894	0.00014620
SDXL	0.00001690	0.00007892	0.00014162	0.00001657
FLUX	0.00009152	0.00008627	0.00008035	0.00005152
VQDM	0.00005064	0.00006152	0.00004454	0.00001033
KD2.1	0.00016612	0.00057640	0.00120155	0.00007604

As shown in the Table 11, consider Image-1 as an example: for lower-capacity models such as SD1.5 and SD2base, the reconstruction loss is on the order of  $10^{-3}$ ; for more advanced models like FLUX [22] and SD3.5 [13], it drops to the order of  $10^{-5}$ . As model performance improves, reconstruction loss continues to decrease, making the loss increasingly sensitive to inherent image complexity. This shift causes greater overlap between the distributions of belonging and non-belonging images.